Billion-pixel x-ray camera (BiPC-X)

Zhehui Wang, Kaitlin Anagnost, Cris W. Barnes, et al.

COLLECTIONS

Paper published as part of the special topic on Proceedings of the 23rd Topical Conference on High-Temperature Plasma Diagnostics

View Online   Export Citation   CrossMark

ARTICLES YOU MAY BE INTERESTED IN

A new class of focusing crystal shapes for Bragg spectroscopy of small, point-like, x-ray sources in laser produced plasmas
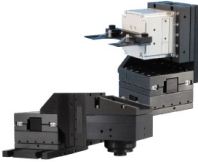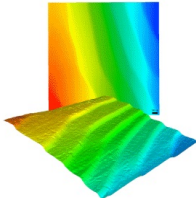Review of Scientific Instruments **92**, 043531 (2021); https://doi.org/10.1063/5.0043599
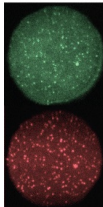
Correction and verification of x-ray imaging crystal spectrometer analysis on Wendelstein 7-X through x-ray ray tracing
Review of Scientific Instruments **92**, 043530 (2021); https://doi.org/10.1063/5.0043513

Effect of irradiation of silicon photodiode arrays for ITER radial x-ray camera investigated by measuring response and current–voltage characteristics
Review of Scientific Instruments **92**, 043301 (2021); https://doi.org/10.1063/5.0031386

Nanopositioning Systems

Modular Motion Control

AFM and NSOM Instruments

Single Molecule Microscopes

MCL MAD CITY LABS INC.
www.madcitylabs.com

Billion-pixel x-ray camera (BiPC-X)

View Online   Export Citation   CrossMark

Zhehui Wang,[1,a)] (iD) Kaitlin Anagnost,[2] Cris W. Barnes,[1] (iD) D. M. Dattelbaum,[1] (iD) Eric R. Fossum,[2] Eldred Lee,[1,2]
Jifeng Liu,[2] J. J. Ma,[3] W. Z. Meijer,[1] (iD) Wanyi Nie,[1] (iD) C. M. Sweeney,[1] (iD) Audrey C. Therrien,[4] (iD)
Hsinhan Tsai,[1] (iD) and Xin Yue[2]

AFFILIATIONS

[1] Los Alamos National Laboratory, Los Alamos, New Mexico 87545, USA
[2] Dartmouth College, Hanover, New Hampshire 03755, USA
[3] Gigajot Technology, Pasadena, California 91107, USA
[4] Université de Sherbrooke, Sherbrooke, Quebec J1K 2R1, Canada

Note: Paper published as part of the Special Topic on Proceedings of the 23rd Topical Conference on High-Temperature Plasma Diagnostics.
[a)] Author to whom correspondence should be addressed: zwang@lanl.gov

ABSTRACT

The continuing improvement in quantum efficiency (above 90% for single visible photons), reduction in noise (below 1 electron per pixel), and shrink in pixel pitch (less than 1 μm) enable billion-pixel x-ray cameras (BiPC-X) based on commercial complementary metal–oxide–semiconductor (CMOS) imaging sensors. We describe BiPC-X designs and prototype construction based on flexible tiling of commercial CMOS imaging sensors with millions of pixels. Device models are given for direct detection of low energy x rays (<10 keV) and indirect detection of higher energies using scintillators. Modified Birks's law is proposed for light yield non-proportionality in scintillators as a function of x-ray energy. Single x-ray sensitivity and spatial resolution have been validated experimentally using a laboratory x-ray source and the Argonne Advanced Photon Source. Possible applications include wide field-of-view or large x-ray aperture measurements in high-temperature plasmas, the state-of-the-art synchrotron, x-ray free electron laser, and pulsed power facilities.

Published under license by AIP Publishing. https://doi.org/10.1063/5.0043013

I. INTRODUCTION

Room-temperature Complementary Metal–Oxide–Semiconductor (CMOS) imaging sensors have entered the single-visible-photon-sensitive regime without avalanche gain.[1] Uses in personal devices such as cell phones and growing applications in machine vision have continuously pushed performance improvements, Fig. 1, and cost reduction for CMOS imaging sensors (CISs). As a result, CISs have gradually taken over charge-coupled device (CCD) imaging sensors over the last decade. Compared with CCDs, which are serial devices and light-induced charge is read out one pixel at a time, row/column by row/column, CISs are based on the parallel pixel architecture with all pixels designed to be exactly the same. Since the electric charge from each pixel can be read out in parallel, CISs are better suited for high-speed applications than CCDs. Consumer CISs have already reached 1000 fps. One of the main results here is that high-performance low-cost visible-light CISs open a door to billion-pixel x-ray camera (BiPC-X) designs, which may find applications such as in wide

field-of-view measurements of high-temperature plasmas, pulsed power facilities, and x-ray scattering experiments in state-of-the-art light sources such as synchrotrons and x-ray free electron lasers. There are several approaches to overcome the low detection efficiency of the visible-light CIS for x-ray photon detection. A multi-layer CIS architecture has been described recently[2,3] and validated with initial x-ray experiments at the Argonne Advanced Photon Source (APS).[4] Another approach is to integrate photon energy attenuation layers (PALs) with CMOS at the pixel level.[6] Alternatively, we may enhance the x-ray efficiency of each CIS by using a scintillator converter. The latter approaches can also be extended to a multilayer configuration.

X-ray bremsstrahlung and characteristic line emissions from impurity ions are signatures of keV and higher temperature plasmas. Recent advances in data-driven science offer new toolboxes such as neural networks to diagnose and understand high-temperature plasmas through three-dimensional (3D) x-ray imaging and tomography.[5] Diffusive x-ray emissions from plasmas and the need to capture a large amount of x-ray data for applications such as training
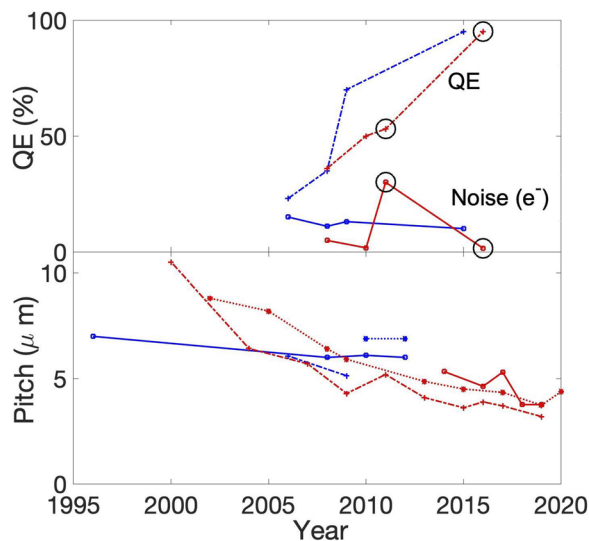
FIG. 1. A brief survey of the evolutionary trends of CCDs (in blue) and CISs (in red) over the last 25 years. The quantum efficiency (QE) for visible photons has now exceeded 90%. The noise level per pixel continues to decline, reaching 1 electron per pixel per readout cycle or less. The individual pixel size or pitch is <5 μm as of 2020. These performance trends, in combination with continuing decline in cost, allow flexibility in BiPC-X camera designs and applications.
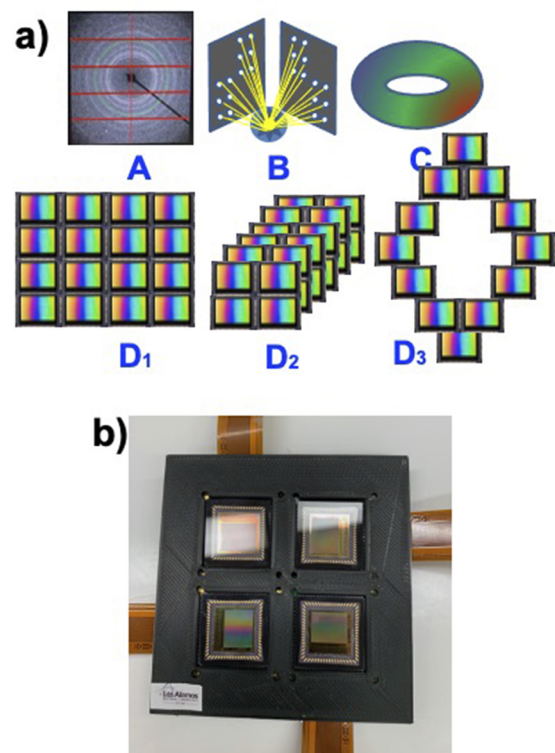

FIG. 2. (a) A BiPC-X may find applications in x-ray diffraction (A), inertial confinement fusion (B), and magnetic fusion (C). Examples of stacking and tiling to form a BiPC-X: planar compact tiling configuration (D_1), stacked tiling (D_2), and distributed tiling (D_3). (b) A laboratory 2×2 tiling prototype using four On Semi Vita 5000 CIS.

of deep neural networks motivate BiPC-X or a giga-pixel x-ray camera instrument. One of the first giga-pixel cameras, AWARE-2, was reported in 2012 for visible light imaging.[7] AWARE-2 used a 16-mm entrance aperture to capture one-giga-pixel images at three frames per minute. The Large Synoptic Survey Telescope (LSST) camera has 3.2×10^9 pixels by tiling 189 CCDs and a 0.5-fps frame rate. A growing number of billion-pixel visible-light cameras have since been reported.

Here, we describe the design studies and initial results toward a BiPC-X. Section II is on the designs based on tiling of commercial CISs with millions of pixels and the prototype construction using 3D printing of a multi-sensor frame. In Sec. III, device models are given for the direct and indirect detection of x-ray photons. It is found that above 10% efficiency can, in principle, be obtained using the CMOS photo-diodes directly for photon energies below 10 keV. Modified Birks's law is proposed for the scintillator light yield.[8] Section IV summarizes the experimental results on sensitivity and resolution. Follow-on work includes application in plasmas and further optimization of BiPC-X prototype design and performance.

II. DESIGN AND PROTOTYPE

Using as building blocks the CIS with millions of pixels (MP), a BiPC-X can be constructed through multi-layer stacking and tiling.[2–4] Several possible configurations are illustrated as D_1, D_2, and D_3 in Fig. 2. The planar compact tiling configuration D_1 increases the x-ray detection aperture, which is proportional to the number of CISs and the individual sensor area. The stacked tiling configuration D_2 increases the aperture for high-energy x rays above 20 keV that can penetrate through multiple layers of CIS.

High-energy x rays and gamma rays (~MeV) are expected from runaway electrons in tokamaks and by nuclear fusion. Configuration D_3 can be used in a toroidal plasma device such as a tokamak or a stellarator. The synchrotron radiation from run-away electrons in a torus as well as the bulk x-ray emissions can be captured by the CMOS sensor arrays surrounding the plasma in the poloidal plane.

There are a large number of commercial CISs to choose from, and they differ in the total number of pixels, pixel pitch, speed, and cost. The latest models offer 10s of MP. Examples include Samsung's ISOCELL Bright HMX sensor (108 MP), Canon 120MXS (122 MP), Gpixel's GMAX3005 (150 MP), OmniVision's OV64C (64 MP), and ON Semiconductor's XGS 45000 (44.7 MP). A 5×5 array of such sensors would be sufficient for a BiPC-X with a pixel resolution of below 1 μm except for GMAX3005 (5.5 μm, rolling shutter) and XGS 45000 (3.2 μm, global shutter). The frame rate of such a BiPC-X would be limited to about 1k fps for now depending on the CIS. For pinhole imaging and tomography of inertial fusion plasmas, the kfps frame rate of such a camera can be compensated by (a) using the gated scintillator and micro-channel plate (MCP) front-end or (b) exposure time gating of the CIS. In both cases, one or several cameras would capture one fast (1 μs or shorter exposure time) x-ray image. A fast x-ray movie would be generated by gating the sensors with different pre-programmed time delays. Additional

customization of the CIS is possible by increasing the x-ray sensitive region. The direct x-ray detection efficiency of the commercial off-the-shelf CIS is below 10%, limited by the pinned photodiode dimension in each pixel to 2–5 μm (the photodiode depth should be larger than 3 μm to ensure red sensitivity[9]) and the small CMOS operating bias voltage of several volts.[10] There is room to substantially increase the photodiode depth to hundreds of micrometers, making such a photodiode efficient for x-ray energies up to 10 keV and thus sufficient for laboratory high-temperature plasmas. CISs are currently manufactured on 200–300 mm Si wafers. A standard 200 mm silicon wafer has a thickness of 725 μm. A 300 mm silicon wafer has a thickness of 775 μm. Current visible light CISs only use a small fraction of the wafer thickness, less than 10 μm.

A laboratory 2 × 2 tiling prototype (21 MP total) using four ON Semi Vita 5000 CISs (5.3 MP, 75 fps, global shutter, 4.8 μm pitch, mono, die thickness 750 μm, glass lid thickness 550 ± 50 μm) has been built, Fig. 2(b). We used a 3D printer (Lulzbot Taz 6) to make the mounting frame for the 4 CISs. The fused filament fabrication printing method used the PolyMax PLA filament (from Polymaker). The thickness of the frame printed is 0.1 in. to allow the detector to slightly protrude beyond the frame. Although the base circuit board is a 1.27 × 1.27 in.², the imaging detector is slightly rectangular and offset from the center of the chip. This requires consideration of how detectors will be oriented (for any size array) to ensure there is adequate room for the attached circuitry. As they are now, the imaging detectors are required to be at least 0.32″ apart to allow room for the boards they are attached to without overlapping with one another. Using the Lulzbot Taz 6 printer, a monolithic frame for up to 8 × 8 (339 MP, Vita 5000) can be printed at once within a few hours. Frames for a BiPC-X are feasible with a larger printer or using a sensor with 16 MP, such as VITA16K from ON Semiconductor.

III. DEVICE MODELS

Here, we describe device models for single x-ray photon detection efficiency and sensitivity. The models provide theoretical basis for BiPC-X component selection and understanding of the component testing data described in Fig. 3 and in Sec. IV, especially the CIS and scintillators.

Device models may be divided into direct detection schemes based on x-ray attenuation in silicon photodiodes in CISs and indirect detection schemes with the primary x-ray attenuators being scintillators. The direct detection is more suitable for x-ray energies up to about 10 keV. The 1/e attenuation length in silicon is 2.7, 17.5, 127, and 962 μm for 1, 5, 10, and 20 keV. Correspondingly, the fraction of x-ray attenuation and therefore the detection efficiency decreases from 82.9%, 24.8%, and 3.9%–0.5% in a silicon pinned photodiode of thickness 5 μm. At 20 keV, the 1/e attenuation length in silicon exceeds the 300 mm silicon wafer thickness of 775 μm.

We consider the planar compact tiling configuration, D$_1$ in Fig. 2, which is sufficient for x-ray energies below 20 keV and plasmas with comparable or lower temperatures. The direct detection model in silicon involves x-ray-to-electron conversion, electron–hole (e–h) cloud propagation, and noise model for the device. In silicon photodiodes, 20 keV x-ray photoelectric (PE) absorption (91.6%) dominates over other processes such as
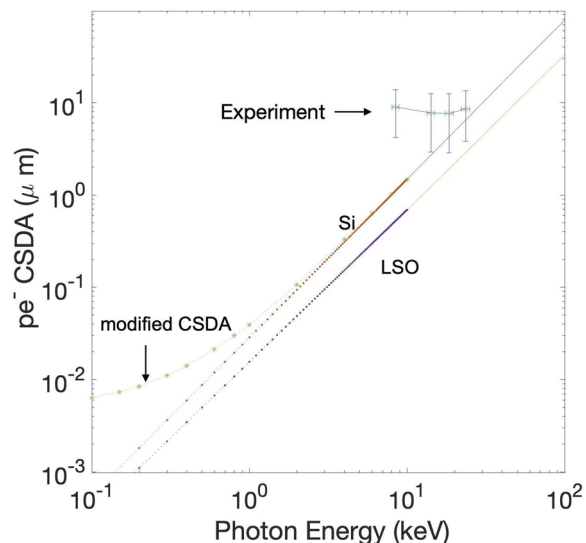

FIG. 3. Photo-electron range in a Si and lutetium oxyorthosilicate (LSO) scintillator as a function of x-ray energy based on the CSDA model. Modification to the CSDA model for Si is also included for $E_X < 10$ keV. Experimental data analysis of a variable energy x-ray source (examples in Fig. 6) indicates that resolution for direct single x-ray photon detection is mainly determined by charge sharing among neighboring pixels. The horizontal error bar corresponds to the energy spread of the x-ray source. The vertical error bar corresponds to a pixel width of 4.8 μm of the Vita 5000 CIS.

Compton scattering (3.1%) and coherent scattering (5.3%). The PE fraction is more than 97% for x-ray energies less than 10 keV. Based on the continuous slowing-down approximation (CSDA)[11] and its modification at lower energies (< 10 keV), Fig. 3, the initial charge (e–h pairs) cloud produced from the energetic electrons (≤20 keV) generated from the PE process does not exceed 4.9 μm, which is comparable to the Vita 5000 CIS pitch of 4.8 μm. Further spread of the charge cloud is due to e–h diffusion in silicon and charge sharing among multiple pixels.[13] The number of e–h pairs created can be estimated as $N_{eh} = E_X/E_0 \pm \sqrt{f_0 E_X/E_0}$ for x-ray energy E_X. E_0 is 3.64 eV, and the Fano factor f_0 is 0.13 for silicon.[12] At $E_X = 5$ keV, for example, $N_{eh} = 1374 \pm 13$. The read noise is 30 e^- in the global shutter mode for Vita 5000 (dynamic range of 53 dB for the full well depth of 13 700 e^-). We conclude that the resolution for direct detection of single x-ray photons is mainly determined by charge sharing among neighboring pixels, as confirmed by using a variable x-ray energy source (Amersham model: AMC 2084, on contact with the sensor for direct detection measurements), Fig. 3.

Next, we consider indirect detection schemes for 10 keV and above energies, when x rays are first turned into a "cloud of visible photons" by using a scintillator. A few relevant scintillators are summarized in Table I. At 20 keV, the 1/e x-ray attenuation lengths are 29.8, 60.9, 91.6 μm, and 22.6 cm for Lu$_2$SiO$_5$(Ce) [LSO (Ce)], ZnO, (C$_6$H$_5$)$_4$PPbBr$_4$ [PPh4PbBr4], and plastic C$_{10}$H$_{11}$ [EJ-228] scintillators, respectively. Except for the plastic scintillator, the smaller 1/e attenuation length than that of silicon at $E_X = 20$ keV may allow thin-film and 2D structures for efficient x-ray conversion, similar to the recent work on PALs.[6]

TABLE I. A comparison of light yield parameters of several scintillators based on a modified Birks's model, Eq. (1).

Scintillator	S (ph/keV)	ρ(g/cm^{-3})	k_1 (μm/keV)
LSO(Ce)	30	7.4	3.2×10^{-2}
ZnO	9.0	5.6	1.5×10^{-2}
PPh4PbBr4	6–8	2.4	0.01–0.1
EJ-228	10.2	1.0	0.13

The relative x-ray response for four different scintillators has been measured using a Hamamatsu R2059 photomultiplier tube (Bialkali 400S photocathode, quartz window, peak QE 27% at 390 nm) and the Argonne Advanced Photon Source (APS) (Fig. 4). The scintillators are a plastic scintillator (EJ-228, 2.5 mm thick, emission peak 391 nm), a ZnO crystal (0.3 mm thick, emission peak 380 nm),[14] a LSO crystal (3 mm thick, emission peak 420 nm), and a perovskite sample PPh4PbBr4 (~1 mm thick, emission peak *est.* at 400 nm). The shape of the pulse is fitted with the function of the form $I = I_0[\exp(-t/t_2) - \exp(-t/t_1)]$ with t_1 and t_2 being the rise and decay time, respectively.

The signals from individual x-ray photons can be estimated as follows: We use the CSDA model to estimate the initial size of the photon cloud generated by photoelectrons. Figure 3 includes an example for LSO. The number of photons emitted is 30 ph/keV for 1 MeV photons in LSO. The photon yield decreases by a factor $f_y < 1$ for lower energy photons. $f_y(E = 30 \text{ keV}) = 0.85$ and $f_y(E = 10 \text{ keV}) = 0.67$ in LSO.[15] At 29.2 keV x-ray photon energy, the average number of photons emitted is about 810. The critical angle is $\theta_c = \text{asin}(1/n) = 0.585$ for n = 1.81. The number of photons collected is about 70. For a QE of 0.3, the final number of
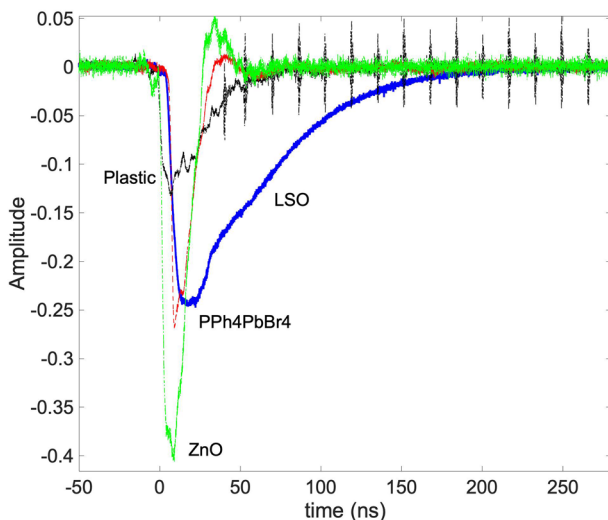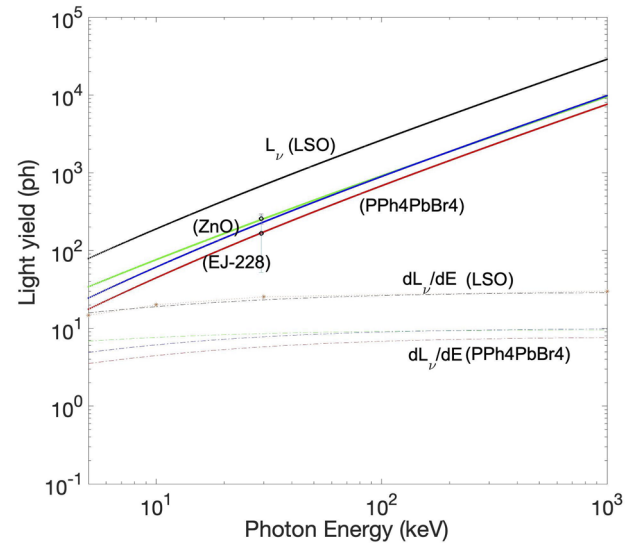
FIG. 5. Light yield model (L_v and dL_v/dE) for x-ray energies from 10 to 1000 keV, when the intrinsic light yield nonproportionality is expected. The known values for LSO and EJ-228 are used to obtain the k_1 values for ZnO and PPh4PbBr4 based on relative light intensities shown in Fig. 4.

x-ray-induced electron–hole pairs is about 20. Some visible photons from a scintillator are lost due to refractive-index mismatching at multiple interfaces before reaching the sensor. The scintillator–CIS cover glass interface could be separated by an air gap. Additional built-in interfaces within a CIS include microlens arrays, light pipes, and antireflection (AR) coating on the silicon surface.[9] Silicon has a large optical refractive index (n) that is wavelength dependent. For example, n is 5.57, 4.65, 4.30, 4.08, and 3.79 at 400, 452, 500, 550, and 689 nm, respectively. Without AR coating, 30%–40% of the incoming light could be lost at the silicon surface alone.

The scintillator light yield (L_v) as a function of x-ray energy uses a modified Birks's model,[8]

$$\frac{dL_v}{dE} = \frac{S}{1 + k_1 \frac{dE}{dx} + k_2 \left(\frac{dE}{dx}\right)^2}, \quad (1)$$

where S is the scintillation efficiency, dE/dx is the energy loss of the particle per path length, and k_1 is Birks's constant and material-dependent. L_v and dL_v/dE are summarized in Fig. 5. The light yield for ZnO and perovskite scintillator PPh4PbBr4 is obtained through relative measurements shown in Fig. 4. The light yield model and results will be useful in further BiPC-X optimization.

IV. SENSITIVITY AND RESOLUTION RESULTS

Single x-ray responses of different CIS models have been characterized using an Amersham variable energy x-ray source (model AMC 2084). Six pairs of K$_\alpha$ and K$_\beta$ lines from Cu, Rb, Mo, Ag, Ba, and Tb are excited by α particles from the ^{241}Am radioisotope. The lowest energy is at Cu K$_\alpha$ 8.04 keV. The highest energy is at Tb K$_\beta$ 50.65 keV. A few examples are shown in Fig. 6. The indirect

FIG. 4. Characterization of the scintillator light yield and decay time using the APS mono-energetic (29.2 keV, Sn K-edge) single-pulse x-ray in the hybrid mode. The rise time and decay time together with the relative light yield have been obtained from the pulse shape analysis.
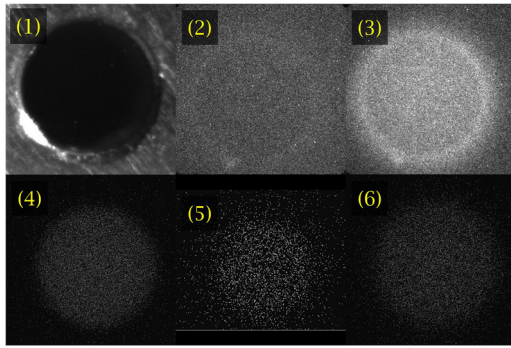
FIG. 6. (1) A photo of the x-ray source aperture (4 mm diameter) used to measure single photon sensitivity. (2) The intensified image of the x-ray source with Cu K_{α} 8.04 keV and K_{β} 8.91 keV. (3) The intensified source image with Tb K_{α}/K_{β}. [(4)–(6)] Direct source images from Ag, Cu, and Tb K_{α}/K_{β} x rays.

detection results are given in panels (2) and (3) for Cu K lines and Tb K lines. An LSO in combination with various CISs did not give results with sufficiently high signal-to-noise ratio (SNR). A single-stage MCP image intensifier was able to improve the SNR as shown. The direct detection results are given in panels (4)–(6). Interactions with individual x-ray photons are clearly visible. The detection efficiency is estimated to be less than 1% and improvements to above 10% are possible through PALs, for example.

Projection x-ray imaging using the direct detection scheme was obtained using the APS synchrotron (ID 10), Fig. 7. Two Vita 5000 CISs were placed in a back-to-back stacked configuration along the x-ray beam path.[4] The Fresnel numbers are 2.4×10^6 and 1.8×10^5 (1 mm spot size) for the front and back CIS, respectively.
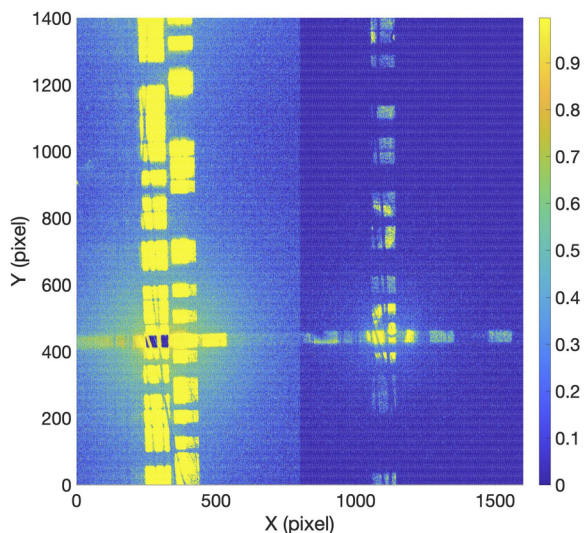

FIG. 7. X-ray images from a random wire pattern on two back-to-back stacked CISs using the APS synchrotron at the Sn K edge (x-ray energy at 29.2 keV). The small rectangles are the spot size of the illumination.

A resolution of 13 μm is obtained from the line-out (y = 435) measurement of Fig. 7.

In summary, we have shown that due to the continuing improvements in quantum efficiency, reduction in noise, and shrinking in pixel pitch, billion-pixel x-ray cameras (BiPC-X) are feasible based on commercial CMOS imaging sensors (CISs) and different tiling configurations. A 2 × 2 planar tiling CMOS camera has been built and tested using both the laboratory x-ray sources and the APS synchrotron. BiPC-X based on direct detection is better suited for x rays below 10 keV. Indirect detection for 10 keV and above will need CISs with single-photon sensitivity or high light yield scintillators. Further work will include data handling and improvements in detection efficiency. Possible applications of BiPC-X include laser-produced and magnetically confined high-temperature plasmas when a few to 10s of keV x rays are isotropically emitted to a large solid angle and difficult to capture with a conventional x-ray camera and a small number of pixels.

ACKNOWLEDGMENTS

DATA AVAILABILITY

The data that support the findings of this study are available from the corresponding author upon reasonable request.

REFERENCES

[1] J. Ma, S. Masoodian *et al.*, Optica **4**, 1474 (2017).

[2] Z. Wang, J. Instrum. **10**, C12013 (2015).

[3] A. Dragone *et al.*, J. Instrum. **11**, C11042 (2016).

[4] X. Li, P. Chu *et al.*, Nucl. Instrum. Methods Phys. Res., Sect. A **942**, 162414 (2019).

[5] X. Yang *et al.*, Sci. Rep. **8**, 2575 (2018).

[6] E. Lee, M. R. James *et al.*, arXiv:2009.00555 (2020).

[7] D. J. Brady, M. E. Gehm *et al.*, Nature **486**, 386–389 (2012).

[8] J. B. Birks, *The Theory and Practice of Scintillation Counting* (Pergamon, 1964).

[9] N. Teranishi, H. Watanabe, T. Ueda, and N. Sengoku, in *Proceedings of the International Electron Devices Meeting* (IEEE, 2012), p. 533.

[10] E. R. Fossum and D. B. Hondongwa, IEEE J. Electron Dev. Soc. **2**, 33 (2014).

[11] M. Tanabashi *et al.*, Particle Data Group, Phys. Rev. D **98**, 030001 (2018).

[12] H. Spieler, *Semiconductor Detector Systems* (Oxford University Press, New York, 2005).

[13] Z. Wang *et al.*, J. Instrum. **13**, C01035 (2018).

[14] C. Hu *et al.*, Nucl. Instrum. Methods Phys. Res., Sect. A **940**, 223 (2019).

[15] B. D. Rooney, J. D. Valentine, and J. Li, IEEE Trans. Nucl. Sci. **45**, 512 (1998).